JOURNAL OF
EMERGING INVESTIGATORS

Article

# A novel calibration algorithm and its effects on heading measurement accuracy of a low-cost magnetometer

**Andy Li[1], Jianhua Liu[2]**

[1] Carroll Senior High School, Southlake, Texas

[2] Embry-Riddle Aeronautical University, Daytona Beach, Florida

## SUMMARY

**The Earth's magnetic heading plays a critical role in numerous applications, including navigation and orientation. The digital compass, which is made with a three-axis magnetometer, has proven to be a very cost-effective tool for providing measurements of the Earth's magnetic heading. To obtain accurate heading measurements for end users, magnetometer calibration is a vital step to mitigate magnetic measurement distortions caused by hard-iron and soft-iron effects. However, current calibration approaches are often complex and lack performance evaluation at different noise levels. In this paper, we present a novel and efficient calibration algorithm that is conceptually simpler than most existing calibration methods and can be easily implemented. We hypothesized that a low-cost magnetometer as used in a smartphone would achieve 1-degree heading measurement accuracy after calibration using our new algorithm. Before applying this new algorithm to real-world data, we verified its effectiveness through numerical simulations. Our study demonstrated that, as the signal-to-noise ratio (SNR) increased, the root-mean-squared errors (RMSEs) of the estimated calibration parameters approached the corresponding Cramer-Rao bounds (CRBs). Experimental results showed that a magnetic heading accuracy of 1.37 degrees was attained for a smartphone located in Texas, U.S.A., which was more accurate than the heading accuracy obtained using the smartphone's internal calibrated data. This study suggests that our calibration approach can allow low-cost magnetometers to provide highly accurate heading measurements, offering a cost-effective solution for various applications, including precise navigation.**

## INTRODUCTION

A digital compass, also known as an electronic compass, is used to indicate the heading of an object relative to the Earth's magnetic field. Unlike traditional compasses that rely on a magnetic needle to point toward the Earth's magnetic north, digital compasses employ a sensor called a magnetometer to measure the Earth's three-dimensional (3D) magnetic field. Based on the magnetometer's measurements, digital compasses use computational algorithms to determine magnetic heading information with greater accuracy compared to traditional compasses. In today's technology-driven world, digital compasses are utilized almost everywhere in our daily lives, whether it be navigating through unfamiliar terrain, orienting maps on our smartphones, or providing heading information for autonomous vehicles. Given the extensive use and our increasing dependence on digital compasses, it is important to understand the accuracy of heading measurements of low-cost devices like those used in smartphones. The required heading accuracy for a digital compass relies on its application. For example, a transport aircraft's heading reference equipment would require higher accuracy than that needed for orienting a smartphone's digital map. In fact, based on RTCA DO-334, the technical standard for the certified heading and attitude reference system used in civil aviation aircraft, the highest heading accuracy requirement under static conditions is 1 degree (i.e., H1 and H2 categories) (1).

To obtain accurate heading measurements from a digital compass, calibration of its magnetometer is essential. The calibration process involves estimating and compensating for errors in sensor's measurements, including hard-iron distortions caused by magnetic sources such as current-carrying wires in the nearby circuits, soft-iron distortions caused by ferromagnetic materials in the vicinity of the magnetometer, and imperfections arising from manufacturing, such as inconsistencies of sensor's material. Therefore, all digital compasses must be calibrated before they are put into practical use.

There are currently two categories of magnetometer calibration methods (2-9). The methods in the first category use dedicated equipment to generate an accurate magnetic field and then estimate the calibration parameters based on the sensor's measurements. During the calibration process, the magnetometer remains stationary at the calibration location. This technique is typically used in factories or laboratories where highly accurate calibrations are needed (2). The methods in the second category calibrate a magnetometer using the Earth's magnetic field. Instead of being stationary like in the first category, the magnetometer is required to rotate in the Earth's 3D magnetic field. Through the 3D motion, the sensor calibration parameters are observable and then can be estimated from the raw measurements obtained during the rotation. The second category's methods are more appealing to application engineers and end users since they do not require any expensive calibration equipment and can be performed almost anywhere on the Earth (3).

Many published papers discuss various algorithms related to the calibration technique in the second category (3-9). A comprehensive review is provided in (3). Additionally, there are calibration algorithms implemented as software tools currently available online (10, 11). However, there are two issues with existing algorithms. First, many of the existing

https://doi.org/10.59720/23-153

calibration algorithms are very complicated. For example, they need to compute Jacobian and Hessian matrices or use Kalman filter frameworks, which are computationally expensive and require prior training to interpret (4, 6, 8). Transforming these sophisticated algorithms into embedded code suitable for real-time systems, like smartphones, is a non-trivial task for end users. Second, the literatures for most of these existing algorithms do not contain rigorous numerical simulation to demonstrate algorithm's performance at different noise levels and to compare their performance against the Cramer-Rao bounds (CRBs), which provide the ultimate performance limits for unbiased estimators (12). Therefore, there is no easy way to see how an algorithm's accuracy changes as the noise level changes.

In this study, we show how we effectively calibrated the raw output from a digital compass's magnetometer to evaluate its heading measurement accuracy. We hypothesized that a smartphone's low-cost digital compass could achieve a high heading measurement accuracy of 1 degree with effective calibration. We first introduced and tested a novel magnetometer calibration algorithm, which is a second-category approach. Unlike existing algorithms that conduct optimization simultaneously for all unknown parameters, our new algorithm decomposes the high-dimensional optimization problem into multiple one-dimensional (1D) optimization problems which makes algorithm implementation much simpler, as it eliminates the need for a high-dimensional optimization algorithm. We then tested the accuracy of our algorithm through numerical simulation experiments. We found that the new algorithm's performance could not reach the estimation accuracy levels defined by CRBs. However, the root-mean-squared errors (RMSEs) of the estimated calibration parameters tended to converge toward the corresponding CRBs of the first-category approach as the signal-to-noise ratio (SNR) increased. Furthermore, we conducted heading accuracy experiments using real-world magnetometer data obtained from a smartphone on a turntable. We applied our new calibration algorithm to the raw measurements collected from the phone and achieved a final heading accuracy of 1.37 degrees. Our study shows that, although the testing result from a magnetometer used in a smartphone does not support our hypothesis of attaining 1-degree accuracy, the final heading accuracy of 1.37 degrees is close to the target value and is noticeably better than the heading accuracy obtained using the smartphone's internal calibrated data. With this level of heading accuracy, new possibilities emerge, enabling applications such as precise navigation without the need for expensive equipment.

## RESULTS

### Numerical Simulation Results

Our new calibration algorithm is essentially a method to deduce a set of deterministic parameters from imprecise measurements. A detailed description on the magnetometer measurement model and the problem statement are provided in Appendix A. Before applying our new algorithm to the real-world data, we intended to understand the algorithm's performance at different noise levels using the numerical simulation method. We evaluated the algorithm's performance by comparing RMSE values obtained by Monte-Carlo simulations against the corresponding CRBs.

Based on the numerical simulation, we observed that the RMSEs of all parameter estimates obtained by the new algorithm came close to their corresponding CRBs as the SNR increased (**Figure 1**). The results showed that the new algorithm performed poorly at the low SNR region (SNR < 30), where the RMSEs of all estimates deviated from the corresponding CRBs (**Figure 1**). The simulation results clearly demonstrated that the new algorithm can accurately estimate all unknown calibration parameters for simulated magnetometer measurements with moderate to high SNRs.

### Real-World Experimental Results

Through real-world experiments, our aim was to test our hypothesis that the magnetometer as used in a smartphone would achieve 1-degree heading measurement accuracy after calibration using our new algorithm. We applied the new calibration algorithm to the magnetometer data collected outdoors from a smartphone (iPhone 13 Pro Max). The calibrated measurements formed a nearly perfect sphere around the origin, which indicated a successful calibration (**Figure 2**). To evaluate the effectiveness of the calibration from another perspective, we also computed the magnitude residuals of the calibrated data. The standard deviation of magnitude residuals for the calibrated data was only about 2.6 milli-Gauss, which was a very small value in comparison to the magnitude of the local magnetic field of 482.1 milli-Gauss at Southlake, TX (13). The small magnitude residuals confirmed the effectiveness of this calibration, especially when compared with magnitude residuals from the smartphone's raw data (**Figure 3**).

We then conducted a heading accuracy test on a homemade turntable. We computed the magnetic heading for each heading station using the calibrated magnetometer data. When we rotated the device for two full revolutions

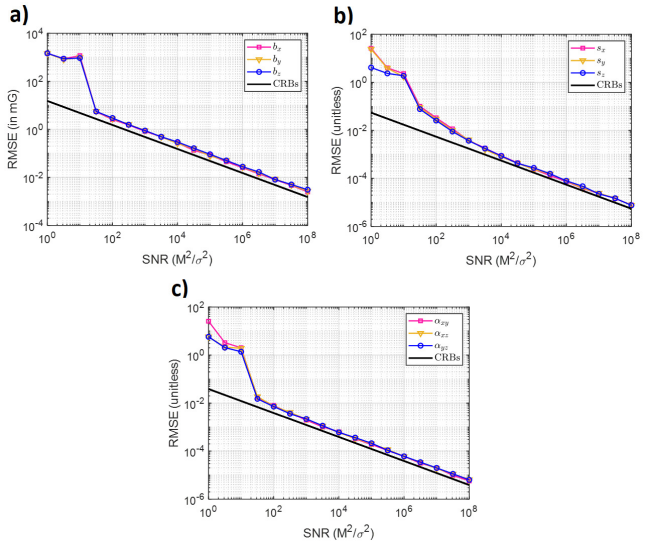


**Figure 1: Comparison of the RMSEs and CRBs for magnetometer calibration parameters obtained using the proposed calibration algorithm.** RMSEs and CRBs for a) bias estimates, b) scale factor estimates, and c) cross-axis coupling term estimates. Note that the x-axis represents the SNR, computed as the square of the overall magnitude of the Earth's magnetic field (M) divided by the variance of the measurement noise (σ), as shown in equation a6 (Appendix A).

https://doi.org/10.59720/23-153

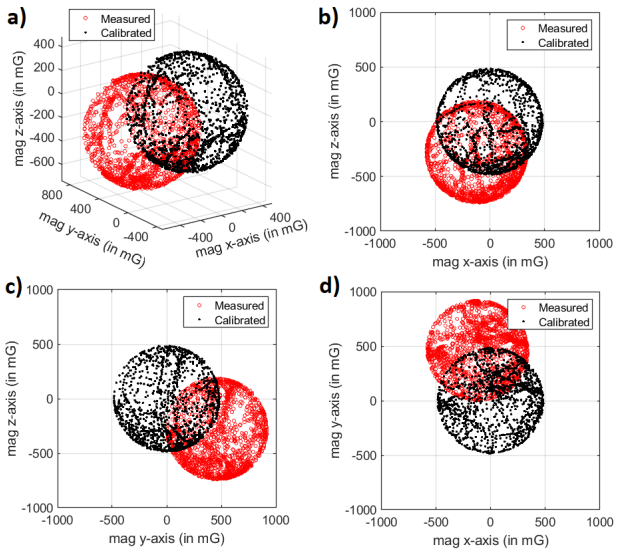


**Figure 2: Calibration results based on real magnetometer data recorded from a smartphone.** The red dots denote the raw sensor data. The black dots denote the calibrated data. The unit of measurement shown in the plots is in milli-Gauss (mG). a) 3D view of the real measurements. b) 2D projection of measurements on mag x and mag z axes. c) 2D projection of measurements on mag y and mag z axes. d) 2D projection of measurements on mag x and mag y axes. The estimated calibration parameters are shown in Table 1.

with a total of 74 heading stations, the maximum heading measurement error was 1.37 degrees, and the two times root-mean-squared (2-RMS) value of the heading errors was 1.2 degrees. Note that the final heading accuracy of 1.37 degrees is very close to the target value and is noticeably better than the heading accuracy of 1.98 degrees obtained by using smartphone internal calibrated data (**Figure 4**).

## DISCUSSION

In this study, we proposed a new calibration algorithm and intended to test the hypothesis that a smartphone's low-cost digital compass could achieve a high heading measurement accuracy of 1 degree with effective calibration. Before applying our new algorithm to the real-world data, we investigated the algorithm's estimation accuracy at different noise levels using the numerical simulation method.

The algorithm's estimation accuracy depends on the magnitude of the applied noise. The lower the noise magnitude, the better the estimation accuracy (i.e., the smaller the RMSE). To characterize the noise level utilized in the simulation, we defined SNR as the division of the square of the overall magnitude of the Earth's magnetic field (numerator) by the variance of the applied measurement noise (denominator), as shown in equation (a6). It should be noted that for a measurement model at a given SNR level, the algorithm's estimation accuracy measured by RMSE is constrained by a fundamental value called the Cramer-Rao bound (CRB). In simple terms, the CRB sets a limit on how precise a parameter can be estimated using a set of observed data that is influenced by noise (12). (For a comprehensive derivation of the CRB, please refer to Appendix B.) It is worth mentioning that the CRB can be derived from the data measurement model. However, knowing the CRB does not mean that one could easily design an estimation algorithm to achieve such an accuracy limit, especially for those high dimensional non-linear estimation problems. Indeed, an important goal for designing an estimation algorithm is to ensure its RMSE (obtained through numerical simulation) are capable of attaining the CRB.

In numerical simulations, we compared the RMSE of the calibration parameter estimate with the CRB. We found that the RMSEs of the calibration parameter estimates suddenly approached the CRBs when the SNR was above a threshold of 30 (**Figures 1a, 1c**). This is because, in the low SNR region, the algorithm failed to provide reliable estimates likely due to the local minimums of the cost function. In fact, our simulation showed that when the SNR was too low, the estimation results failed to converge to a stable value even after reaching the maximum number of iterations (set to 200 in our test). Once the SNR is high enough and passes the threshold, our calibration algorithm can provide meaningful estimates with accuracies that are very close to the corresponding CRBs. Typically, the estimation results converged within 20 iterations. As will be discussed later, the SNR for the real-world measurements is usually much higher than 30. It should be noted that understanding the algorithm behavior at the low SNR region remains important, and further investigation on how to improve algorithm performance at the low SNR region is considered as a future direction for this study.

Interestingly, we also observed a slight gap between the RMSE lines from the simulation results and the corresponding CRB lines (**Figure 1**). This is likely because the derivation of the CRB falls under the first category of calibration approaches, which assume that the magnetic field inputs on all three axes are known in order to simplify the derivation. In contrast, our algorithm relies solely on the knowledge that the magnitude of the magnetic field is a known constant. Due to the limited information on the magnetic field inputs, our algorithm does not produce as optimal results as CRBs, but the difference is small especially in the high SNR region. It is possible to use known magnetic input data to calibrate the magnetometer. However, using known magnetic inputs for calibration falls into the first category of magnetometer calibration methods as discussed in the introduction. We do

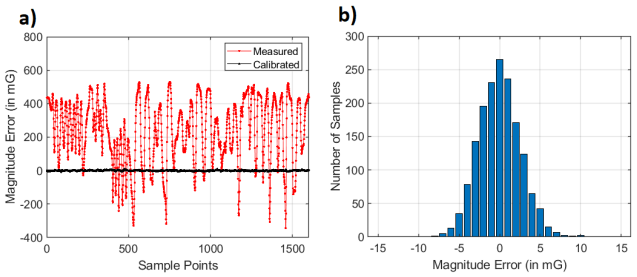


**Figure 3: Magnitude differences (i.e., residuals) between the magnetometer data and the reference magnetic field strength of 482.1 milli-Gauss.** (a) The red line denotes the magnitude difference from the raw data. The black line denotes the magnitude difference from the calibrated data. (b) Histogram of the calibrated data magnitude residuals as shown in the black line in (a). The standard deviation for magnitude residuals from the calibrated data is about 2.6 milli-Gauss.

https://doi.org/10.59720/23-153

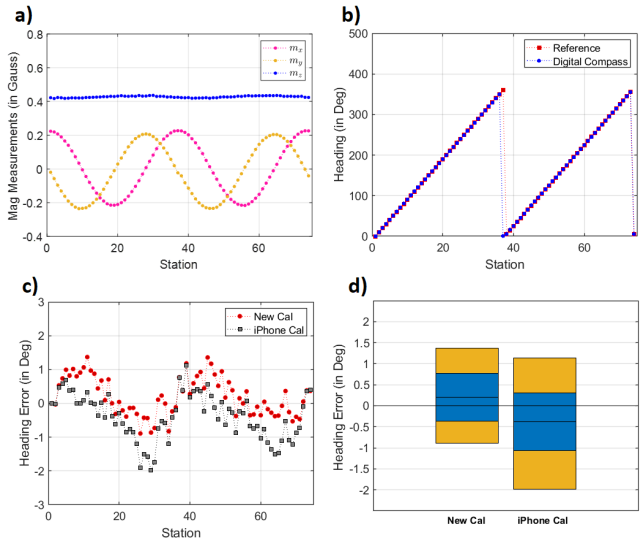


**Figure 4: Heading accuracy based on the calibrated magnetometer data from a smartphone.** (a) The 5-seconds-averaged magnetometer data (after calibration) at 74 different heading stations. The heading stations are separated by 10 degrees (deg). (b) The estimated magnetic headings from the magnetometer against the reference headings. Note that we have subtracted the computed magnetic headings with an offset value so that the heading output from the magnetometer at the first station is exactly 0 degrees. (c) The headings errors from the magnetometer. Using our calibrated data, we found that the maximum heading error was 1.37 degrees, and the 2-RMS value was 1.2 degrees, denoted as the "New Cal". Conversely, with the smartphone's internally calibrated data, we observed a maximum heading error of 1.98 degrees and a 2-RMS value of 1.57 degrees, labeled as the "iPhone Cal". (d) Comparisons of the mean, the standard deviation, the minimum, and the maximum of heading errors between those obtained from our calibrated results (i.e., New Cal) and those from smartphone internal calibrated results (i.e., iPhone Cal) as shown in (c). Blue blocks indicate the span of standard deviation and gold blocks indicate the span of minimum and maximum errors.

not consider those methods in this study since they rely on specialized equipment to generate a precise magnetic field. A separate study could be conducted for first category of magnetometer calibration methods in the future.

Although our algorithm provides sub-optimal results, the RMSEs can be very small in practical applications if the SNR is high enough, as demonstrated in the numerical simulations. For example, when calibrating a magnetometer in the Earth's magnetic field in the continental United States, the Earth's magnetic strength is about 0.5 Gauss. Moreover, we conservatively assume that the standard deviation of sensor measurement noise is 4 milli-Gauss. With that, we can have a SNR level of $1.56 \times 10^4$ (i.e., $(0.5/0.004)^2$, see equation (a6)) for the raw measurements. At this practical SNR level, our new algorithm is capable of providing very accurate estimates for all calibration parameters (**Figure 1**).

For the real-world experiment, we used an iPhone 13 Pro Max for magnetometer data collection. The raw magnetometer data were significantly distant from the origin, which was due to the strong hard-iron distortions from the phone. Note also that the calibrated data showed a nearly perfect sphere shape around the origin (**Figure 2**). Since the standard deviation of magnitude residuals for calibrated data was about 2.6 milli-Gauss and the local Earth's magnetic field strength at Southlake, Texas was 482.1 milli-Gauss, this corresponded to a SNR of about $3.4 \times 10^4$ which was sufficient to generate accurate estimates for all calibration parameters based on our simulation study (**Figure 1**). The calibration parameters converged in 10 iterations using the new calibration algorithm. Inspecting the estimated hard-iron and soft-iron calibration parameters from this test, we noticed the significant $b_y$ value of 0.46 Gauss and the scale factor term $s_y$ of 0.94, along with small cross-axis coupling terms described in Appendix A (**Table 1**). Note that $b_y$ represents the hard-iron offset along the y-axis, and the term $s_y$ denotes scale factor for the y-axis, with a nominal value of one. Their values indicated the presence of substantial hard- and soft-iron errors in the raw magnetometer data, likely introduced by internal hardware components within the iPhone.

We observed from the heading accuracy test results that the maximum heading measurement error using the calibrated magnetometer data was 1.37 degrees, and the 2-RMS value was 1.2 degrees. For comparison, we computed heading values based on the smartphone's internal calibrated magnetometer data that were simultaneously recorded with the raw data during the heading accuracy test. Using that data, we found the maximum heading measurement error to be 1.98 degrees with a 2-RMS value of 1.57 degrees (**Figure 4**). It is clear from this experiment that our calibration is more accurate than that of the smartphone (**Figure 4d**). We noticed that the final heading errors seem to have a systematic pattern with stations (**Figure 4c**). It is worth noting that a portion of the errors from the heading accuracy test could be due to imprecision when manually aligning the smartphone at a given heading station on the homemade turntable. In the future, we plan to use more precise reference systems, such as a computer-controlled turntable, for the heading accuracy test. We also computed heading results based on the raw magnetometer data. However, the raw data contained significant hard-iron errors, making it unsuitable for deriving any meaningful heading values; because of that, the corresponding heading results were not provided here. According to DO-334, the heading accuracy is evaluated

| | $b_x$ (Gauss) | $b_y$ (Gauss) | $b_z$ (Gauss) | $s_x$ | $s_y$ | $s_z$ | $\alpha_{xy}$ | $\alpha_{xz}$ | $\alpha_{yz}$ |
|---|---|---|---|---|---|---|---|---|---|
| **Row #1** | 0.50 | -0.40 | 0.30 | 1.1 | 1.2 | 1.3 | 0.10 | -0.12 | 0.080 |
| **Row #2** | -0.12 | 0.46 | -0.28 | 0.95 | 0.94 | 0.95 | -0.0074 | 0.00030 | -0.0030 |

**Table 1: Hard-iron and soft-iron parameters.** Row #1 shows the predefined hard-iron and soft-iron parameters that are used for numerical simulation. Row #2 shows the estimated hard-iron and soft-iron calibration parameters based on the real magnetometer data from a smartphone.

https://doi.org/10.59720/23-153

as either maximum or 2-RMS of the measurement errors, whichever is larger (1). From that, we conclude that our test results do not support our original hypothesis of 1-degree accuracy. Nevertheless, the heading accuracy of 1.37 degrees from our test was close to the target value and, in fact, met the H3 category of 1.5 degrees accuracy as defined in DO-334. These results show the promise that our calibration approach allows low-cost magnetometers to provide highly accurate heading measurements in the real world.

## MATERIALS AND METHODS

### New Calibration Algorithm

It can be seen from equations (a7) and (a8), as shown in Appendix A, that the task here is to solve an optimization problem with a total of nine unknown parameters. Instead of optimizing all parameters simultaneously, our new method conducted the optimizing process sequentially on each parameter and iterated the process until results converged. The detailed algorithm steps are outlined as follows.

**Step #1:** Initialization. Set the estimates for the bias terms $b_x$, $b_y$, and $b_z$ to 0, set estimates for $k_x$, $k_y$, and $k_z$ to 1, and set estimates for $\beta_{xy}$, $\beta_{xz}$, and $\beta_{yz}$ to 0.
**Step #2:** Fixing all other estimation parameters, optimize $b_x$ by conducting a 1D search based on equation (a8). Once the optimal $b_x$ (i.e., the one that minimizes the cost function J) is found, update the current estimate for $b_x$ and then repeat the same process for $b_y$ and $b_z$.
**Step #3:** With the updated estimates, apply the same process as described in **Step #2** to estimate $k_x$, $k_y$, and $k_z$.
**Step #4:** Apply the same process as described in **Step #3** to estimate $\beta_{xy}$, $\beta_{xz}$, and $\beta_{yz}$.
**Step #5:** Iterate **Steps #2** to **#4** until all estimates converge or the predefined maximum iteration number has been reached.

Below are a few remarks regarding our new algorithm.
1) We optimized the bias terms first, followed by the scale factor terms, and lastly the misalignment terms. This sequencing was based on our empirical experience, and our numerical simulations confirmed that this sequence produced the most favorable optimization results.
2) Instead of optimizing $s_x$, $s_y$, $s_z$, $\alpha_{xy}$, $\alpha_{xz}$, and $\alpha_{yz}$, the algorithm conducted 1D optimization on $k_x$, $k_y$, $k_z$, $\beta_{xy}$, $\beta_{xz}$, and $\beta_{yz}$ so that matrix inversion operation can be avoided during the compensation step. Once $k_x$, $k_y$, $k_z$, $\beta_{xy}$, $\beta_{xz}$, and $\beta_{yz}$ are obtained, $s_x$, $s_y$, $s_z$, $\alpha_{xy}$, $\alpha_{xz}$, and $\alpha_{yz}$ can be easily recovered by a matrix inverse operation.
3) For 1D optimization, we used the golden-section search approach (14). The search stopped when the absolute change (as compared with the previous result) was less than $10^{-7}$.
4) The optimization ranges for $b_x$, $b_y$, and $b_z$ were set from -2 to 2 Gauss. The optimization ranges for $k_x$, $k_y$, and $k_z$ were set from 0 to 2. The optimization ranges for $\beta_{xy}$, $\beta_{xz}$, and $\beta_{yz}$ were set from -1 to 1.
5) The maximum iteration number was set as 200. The iterations also stopped when the sum of absolute changes (as compared with the results obtained from the previous iteration) for all parameters was less than $10^{-6}$.

It is noteworthy that the new algorithm does not require any sophisticated math operations such as the computation of the derivative terms of the cost function. It only needs a simple 1D numerical search for a local minimum, which can be implemented easily.

### Numerical Simulation Setup

During the numerical simulation process, we first identified a set of input parameters, such as hard-iron, soft-iron, and scale factor terms, that can influence the outcome of the magnetometer measurements (**Table 1**). Next, we generated the magnetometer measurements using the measurement model described in equation (a1). To simulate the imprecise measurements commonly obtained in the real world, we added random noise generated from a known Gaussian probability distribution to these measurements. Using the measurements affected by random noise as the input, we ran the new calibration algorithm to compute the output of a total of nine magnetometer calibration parameters as defined in equation (a1). Once the simulation finished running, we gathered the estimated calibration parameters and compared them with the truth reference values to obtain the estimation error for each parameter. It is important to note that the estimation error of each parameter is also a random variable influenced by the applied random noise. Therefore, to assess the statistical properties of those estimation errors, we need to run the simulation multiple times. After repeating the simulation process for a large number of times (set to 200 in our test), with the random noise generated and applied each time, we then computed RMSE for each parameter based on the estimation errors from all trials. The RMSE value is crucial in the context of the numerical simulation since it serves as a metric for evaluating the estimation accuracy of the new algorithm. A smaller RMSE value indicates a higher degree of estimation accuracy. Note also that the above simulation

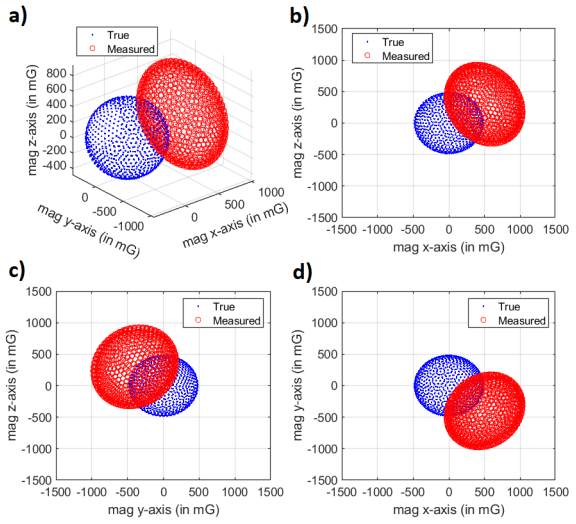


**Figure 5: Simulated noise-free magnetometer measurements used to test the new calibration algorithm.** Blue dots denote 1000 points of truth measurements that are evenly distributed on a sphere with a radius of 482.1 milli-Gauss (mG). Red dots denote the measured magnetometer outputs that are distorted by the soft-iron and hard-iron effects with parameters listed in Table 1. a) 3D view of the simulated measurements. b) 2D projection of measurements on mag x and mag z axes. c) 2D projection of measurements on mag y and mag z axes. d) 2D projection of measurements on mag x and mag y axes.

https://doi.org/10.59720/23-153

approach is commonly referred to as a Monte-Carlo simulation, as the method relies on randomness, probability, and a substantial number of trials, much like games of chance at the famous Monte-Carlo Casino in Monaco.

The numerical simulation was conducted using MATLAB® (version 2023a). We used an open-source MATLAB script to compute 1000 points of truth measurements that are evenly distributed on a sphere (**Figure 5**) (15). The magnetic field strength (i.e., the radius of the sphere) was set as 482.1 milli-Gauss to match the local magnetic field strength in Southlake, Texas. Based on the predefined nine sensor error parameters, distorted measurements without noise were generated based on equation (a1) (**Table 1, Figure 5**). At each SNR level, 200 experiments were conducted with independent random Gaussian noise being applied to each experiment. The RMSE values for each parameter were computed based on the estimation results from those 200 experiments.

### Real-World Experimental Setup

An iPhone 13 Pro Max with an iOS app named "Sensor Play – Data Recorder" was used to collect real-world magnetometer data (16). The app offers two sets of outputs from the iPhone's magnetometer: the raw values and the calibrated values. To make our testing results independent of the iPhone's internal calibration scheme, we only applied our calibration algorithm to the raw values. The magnetometer data were sampled at 25 Hz. We collected data for the calibration data set for about 50 seconds while standing in an outdoor football field and rotating the iPhone by hand for all possible orientations.

After we obtained the estimated hard-iron and soft-iron calibration parameters from the calibration data set, we conducted a heading accuracy test using a homemade turntable, which was a wooden box made of plywood with dimensions of 13 inches (L) x 10 inches (W) x 4 inches (H) (**Figure 6**). In our experiment, the turntable and the attached compass protractor were fixed to the ground. The smartphone was positioned in various orientations, guided by the markers on the compass protractor. We set up the turntable in a magnetically clean environment where there were no ferrous materials present. The top of the turntable was carefully leveled by using a bubble level. We then manually set the iPhone's heading for two full revolutions with a total of 74 stations based on the mark of the compass protractor. The first revolution was from 0 to 360 degrees with a station every 10 degrees apart (37 stations) and the second revolution was from 5 degrees to 365 degrees with a station every 10 degrees apart (37 stations). At each station, the iPhone was kept stationary for about 7 seconds. We used 5-second-long averaged data per station for heading computation.

Based on the calibration parameters obtained in the previous step, the raw data collected from the turntable were compensated to obtain the hard-iron and soft-iron distortion-free measurements. To compute a magnetic heading from the 3D magnetometer data, the measurements from the magnetometer need to be obtained in the local level frame, which is the coordinate system that is parallel to the Earth's local tangent. Although the top surface of our turntable aligned with the local level frame, placing the smartphone on the table may introduce slight misalignments between the magnetometer body axis frame and the top surface of the turntable. For an accurate heading estimate, we need to account for those small malignments. With a valid misalignment compensation, the down component (i.e., $m_z$) and the horizontal component (i.e., $\mathrm{sqrt}(m_x^2 + m_y^2)$ ) of the magnetometer measurement should be constant values that are independent of heading orientation (7). Using this fact, we estimated the pitch misalignment angle as 0.57 degrees and the roll misalignment angle as -1.93 degrees for our test setup. The method for estimating pitch and roll misalignment angles is described in detail in Appendix C. Once we compensated those misalignments in the calibrated data from the heading accuracy test, the magnetic heading can be computed using the formula of

$$\varphi = -\tan^{-1}\left(\frac{m_y^l}{m_x^l}\right),$$

where $m_x^l$ and $m_y^l$ indicate magnetometer x-axis and y-axis measurements, respectively, in the local level frame (7). For the final heading accuracy evaluation, instead of directly comparing the measured magnetic heading against a ground truth of the magnetic heading, which is hard to obtain, we accessed the relative change between the measured magnetic heading and the first reference heading point. The ground truth for the relative change of the measurement magnetic heading was determined by the markers on the compass protractor affixed to the turntable.

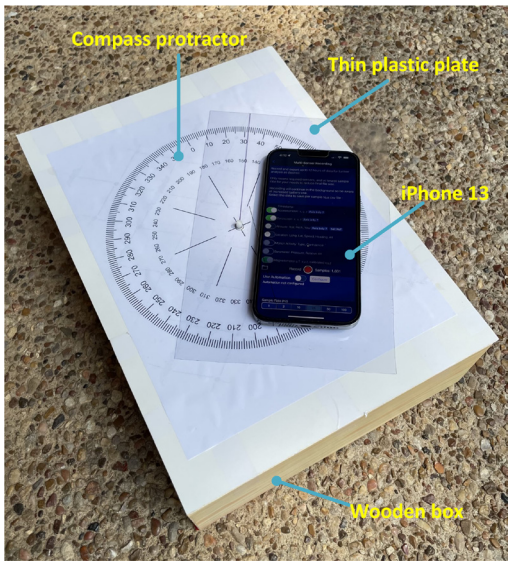


**Figure 6: The real-word experiment setup.** An iPhone 13 Pro Max with an app called "Sensor Play – Data Recorder" (by Philip Broder) is used to collect data on top of a homemade turntable, which is a wooden box made of plywood with dimensions of 13 inches (L) x 10 inches (W) x 4 inches (H). The iPhone was attached to a thin plastic plate using adhesive stickers. The thin plastic plate could pivot freely on the top of the turntable, rotating about the center of the compass protractor. Using the marker line drawn on the thin plastic plate, we were able to manually align the plastic plate and the attached iPhone to the desired heading marks on the compass protractor.

## ACKNOWLEDGMENTS

We would like to express our appreciation to Mr. Leafgreen and Mr. Olson, two teachers who provided feedback and always supported this project. We also express our appreciation to the reviewers and editors for their valuable comments and suggestions, which enhanced the quality of

https://doi.org/10.59720/23-153

our research work.

**Received:** July 7, 2023
**Accepted:** November 3, 2023
**Published:** January 25, 2024

## REFERENCES

1. "RTCA DO-344, Minimal Operational Performance Standards (MOPS) for Strapdown Attitude and Headings Reference Systems (AHRS)." *The Radio Technical Commission for Aeronautics*. www.rtca.org. Accessed 27 Jun. 2023.
2. Bronaugh, E. L. "Helmholtz coils for calibration of probes and sensors: limits of magnetic field accuracy and uniformity." *Proceedings of International Symposium on Electromagnetic Compatibility*, Atlanta, GA, USA, 1995, doi: 10.1109/ISEMC.1995.523521.
3. Papafotis, Konstantinos, et al. "Magnetic Field Sensors' Calibration: Algorithms' Overview and Comparison." *Sensors*, vol. 21, no. 16, Jun. 2021, https://doi.org/10.3390/s21165288.
4. Wu, Helong, et al. "An improved magnetometer calibration and compensation method based on Levenberg–Marquardt algorithm for multi-rotor unmanned aerial vehicle." *Measurement and Control*. vol. 53, issue 3-4, Jan. 2020, https://doi.org/10.1177/0020294019890627.
5. Kok, M. and Schön, T. B. "Magnetometer Calibration Using Inertial Sensors." IEEE Sensors Journal, vol. 16, no. 14, Jul. 2016, https://doi.org/10.1109/JSEN.2016.2569160.
6. Yigitler, H., and Leblebicioğlu M. K. "Online Calibration of Strapdown Magnetometers." *IFAC Proceedings Volumes*, vol. 42, no. 16, 2009, https://doi.org/10.3182/20090909-4-JP-2010.00116.
7. Gebre-Egziabher, D., et al. "Calibration of strapdown magnetometers in magnetic field domain." *Journal of Aerospace Engineering*, vol. 19, no. 2, Apr. 2006, https://doi.org/10.1061/(ASCE)0893-1321(2006)19:2(87).
8. Vasconcelos, J. F., et al. "Geometric Approach to Strapdown Magnetometer Calibration in Sensor Frame." *IEEE Transactions on Aerospace and Electronic Systems*, vol. 47, no. 2, Apr. 2011, https://doi.org/10.1109/TAES.2011.5751259.
9. Wu, Y., and Shi, W. "On Calibration of Three-Axis Magnetometer." *IEEE Sensors Journal*, vol. 15, no. 11, Nov. 2015, https://doi.org/1109/JSEN.2015.2459767.
10. "Adafruit SensorLab - Magnetometer Calibration." *Adafruit*. learn.adafruit.com/adafruit-sensorlab-magnetometer-calibration?view=all. Accessed 6 Jun. 2023.
11. "Magnetometer Calibration." www.mathworks.com/help/fusion/ug/magnetometer-calibration.html. Accessed 6 June 2023.
12. Casella, G., and Berger, R.L., "Chapter 7: Point Estimation." *Statistical Inference*, edited by Carol Reitz and Carolyn Crockett, 2nd ed., Duxbury Press, 2002, pp. 335-341.
13. "Magnetic Field Calculators." *National Oceanic and Atmospheric Administration*. www.ngdc.noaa.gov/geomag/calculators/magcalc.shtml?model=igrf#igrfwmm. Accessed 6 Jun. 2023.
14. Press, W. H., et al. "Section 10.2. Golden Section Search in One Dimension." *Numerical Recipes: The Art of Scientific Computing*, 3rd ed., New York: Cambridge University Press, 2007, pp. 492-495.
15. "MATLAB functions to perform uniform sampling of a sphere." *MathWorks File Exchange*. www.mathworks.com/matlabcentral/fileexchange/37004-suite-of-functions-to-perform-uniform-sampling-of-a-sphere. Accessed 19 Sept. 2023.
16. Broder, Philip., "Sensor Play – Data Recorder" Apple iOS app. Accessed 19 September 2023.
17. Stoic, P. and Moses, R., "Cramer-Rao Bound Tools", *Introduction to Spectral Analysis*, Upper Saddle River, NJ: Prentice-Hall 1997, pp. 285-295.
18. Stevens, Brian L., et al. "Matrix analysis of kinematics", *The Kinematics and Dynamics of Aircraft Motion*, Third Edition, Oct. 2015, pp. 25-27.

# APPENDICES

## A. Data Model for Magnetometer Measurements

Assume that $N$ independent measurements are taken from a three-axis (denoted as $x$, $y$, and $z$ axis) magnetometer device. The measurements can be modeled as

$$\begin{bmatrix} x(n) \\ y(n) \\ z(n) \end{bmatrix} = \begin{bmatrix} s_x & \alpha_{xy} & \alpha_{xz} \\ \alpha_{xy} & s_y & \alpha_{yz} \\ \alpha_{xz} & \alpha_{yz} & s_z \end{bmatrix} \cdot \begin{bmatrix} m_x(n) \\ m_y(n) \\ m_z(n) \end{bmatrix} + \begin{bmatrix} b_x \\ b_y \\ b_z \end{bmatrix} + \begin{bmatrix} e_x(n) \\ e_y(n) \\ e_z(n) \end{bmatrix}, \quad n = 1,2,\dots,N \tag{a1}$$

where $b_x$, $b_y$, and $b_z$ are bias terms for each sensing axis; $s_x$, $s_y$, and $s_z$ are scale factor terms; $\alpha_{xy}$, $\alpha_{xz}$, and $\alpha_{yz}$ are for misalignment or cross-axis coupling terms; $m_x(n)$, $m_y(n)$, and $m_z(n)$ are the Earth's current magnetic field projected onto each magnetometer sensing axis; and $e_x(n)$, $e_y(n)$, and $e_z(n)$ are measurement noise terms and are assumed as zero-mean Gaussian random variables with a variance of $\sigma^2$ (3).

To help understand the magnetometer measurement model, equation (a1) is briefly explained as follows. First, consider only the x-axis. Without the Earth's magnetic field, the sensor's reading will be just $b_x$, which is the hard-iron distortion generated by the circuits around the sensor. Next, without effects from the hard-iron distortion, the sensor's reading from the Earth's magnetic field is $s_x \cdot m_x(n) + \alpha_{xy} \cdot m_y(n) + \alpha_{xz} \cdot m_z(n)$, where $s_x$, $\alpha_{xy}$, and $\alpha_{xz}$ can be introduced by soft-iron distortion when the sensor is close to a ferromagnetic material, such as an iron object. By superposition and considering noise, we have

$$x(n) = s_x \cdot m_x(n) + \alpha_{xy} \cdot m_y(n) + \alpha_{xz} \cdot m_z(n) + b_x + e_x(n). \tag{a2}$$

Similar derivations can be used to obtain y-axis and z-axis measurements as

$$y(n) = s_y \cdot m_y(n) + \alpha_{xy} \cdot m_x(n) + \alpha_{yz} \cdot m_z(n) + b_y + e_y(n), \tag{a3}$$

and

$$z(n) = s_z \cdot m_z(n) + \alpha_{xz} \cdot m_x(n) + \alpha_{yz} \cdot m_y(n) + b_z + e_z(n). \tag{a4}$$

Equations (a2) to (a4) above can be generalized to a matrix formation as shown in equation (a1). We can also see from equations (a2) to (a4) that, due to the hard-iron and soft-iron effects, the sensor outputs can no longer truthfully represent the measurements of the Earth's 3D magnetic field. Therefore, without proper calibration and compensation, error will be introduced to the heading estimation.

The goal for the calibration algorithm is to find nine unknown parameters of $b_x$, $b_y$, $b_z$, $s_x$, $s_y$, $s_z$, $\alpha_{xy}$, $\alpha_{xy}$, and $\alpha_{xy}$ based on $N$ raw measurements of $x(n)$, $y(n)$, and $z(n)$. Note that the applied the Earth's magnetic field on each sensing axis is unknown. However, the overall magnitude of the Earth's magnetic field, $M$, is typically known and is assumed to be constant at the place of the calibration. The magnitude of the Earth's magnetic field can be defined as

$$M \triangleq \sqrt{m_x^2(n) + m_y^2(n) + m_z^2(n)}\ . \tag{a5}$$

In this study, we define the signal-to-noise ratio (SNR) as

$$\mathrm{SNR} \triangleq \frac{M^2}{\sigma^2}\ , \tag{a6}$$

where $\sigma^2$ is the variance of the measurement noise. If we assume all the nine calibration parameters are estimated, the calibrated measurements can be obtained by the reversed operation in equation (a1) as

$$\begin{bmatrix} \hat{m}_x(n) \\ \hat{m}_y(n) \\ \hat{m}_z(n) \end{bmatrix} = \begin{bmatrix} k_x & \beta_{xy} & \beta_{xz} \\ \beta_{xy} & k_y & \beta_{yz} \\ \beta_{xz} & \beta_{yz} & k_z \end{bmatrix} \cdot \left( \begin{bmatrix} x(n) \\ y(n) \\ z(n) \end{bmatrix} - \begin{bmatrix} b_x \\ b_y \\ b_z \end{bmatrix} \right), \quad n = 1,2, \dots, N \tag{a7}$$

where $\begin{bmatrix} k_x & \beta_{xy} & \beta_{xz} \\ \beta_{xy} & k_y & \beta_{yz} \\ \beta_{xz} & \beta_{yz} & k_z \end{bmatrix}$ is the inverse of $\begin{bmatrix} s_x & \alpha_{xy} & \alpha_{xz} \\ \alpha_{xy} & s_y & \alpha_{yz} \\ \alpha_{xz} & \alpha_{yz} & s_z \end{bmatrix}$ and is also a symmetric 3x3 matrix.

As shown in reference (3), with a given set of raw measurements, we can estimate the nine unknown parameters by minimizing the following cost function:

$$J \triangleq \sum_{n=1}^{N} \left[ \hat{m}_x^2(n) + \hat{m}_y^2(n) + \hat{m}_z^2(n) - M^2 \right]^2 \tag{a8}$$

Note that the above optimization problem is equivalent to a sphere-fitting problem. Note also that we need to have varied values of $m_x(n)$, $m_y(n)$, and $m_z(n)$ to avoid the singularity problem in parameter estimation. This means we need the magnetometer to face different directions when collecting calibration data.

**B. Derivation of CRBs**

The Cramer-Rao bound (CRB) is a powerful statistical tool that relates to the estimation of a deterministic parameter. To make this paper self-contained, we provide derivations on this important tool based on the data model as provided in equation (a1).

Define

$$\mathbf{e}(n) \triangleq [e_x(n) \quad e_y(n) \quad e_z(n)]^T, \tag{b1}$$

$$\mathbf{m}(n) \triangleq [m_x(n) \quad m_y(n) \quad m_z(n)]^T, \tag{b2}$$

$$\mathbf{b} \triangleq [b_x \quad b_y \quad b_z]^T, \tag{b3}$$

$$\mathbf{T} \triangleq \begin{bmatrix} s_x & \alpha_{xy} & \alpha_{xz} \\ \alpha_{xy} & s_y & \alpha_{yz} \\ \alpha_{xz} & \alpha_{yz} & s_z \end{bmatrix}, \tag{b4}$$

$$\mathbf{x}(n) \triangleq [x(n) \quad y(n) \quad z(n)]^T, \tag{b5}$$

where $(\cdot)^T$ denotes transpose. Then equation (a1) can be expressed in matrix format as

$$\mathbf{x}(n) = \mathbf{T}\mathbf{m}(n) + \mathbf{b} + \mathbf{e}(n), \ n = 1,2, \dots, N. \tag{b6}$$

Also define

$$\boldsymbol{\theta} \triangleq [b_x \quad b_y \quad b_z \quad s_x \quad s_y \quad s_z \quad \alpha_{xy} \quad \alpha_{xz} \quad \alpha_{yz}]^T \tag{b7}$$

as the vector for all nine unknown parameters. Here, we assume $\mathbf{m}(n)$ is known to simplify the derivation.

Let

$$\boldsymbol{\mu}(n) \triangleq \mathbf{T}\mathbf{m}(n) + \mathbf{b} \ . \tag{b8}$$

It is easy to verify that derivatives of $\boldsymbol{\mu}(n)$ with respect to each unknown parameter can be expressed as

$$\frac{\partial \boldsymbol{\mu}(n)}{\partial b_x} = [1 \quad 0 \quad 0]^T, \tag{b9}$$

$$\frac{\partial \boldsymbol{\mu}(n)}{\partial b_y} = [0 \quad 1 \quad 0]^T, \tag{b10}$$

$$\frac{\partial \boldsymbol{\mu}(n)}{\partial b_z} = [0 \quad 0 \quad 1]^T \ , \tag{b11}$$

$$\frac{\partial \boldsymbol{\mu}(n)}{\partial s_x} = [m_x(n) \quad 0 \quad 0]^T, \tag{b12}$$

$$\frac{\partial \boldsymbol{\mu}(n)}{\partial s_y} = [0 \quad m_y(n) \quad 0]^T, \tag{b13}$$

$$\frac{\partial \boldsymbol{\mu}(n)}{\partial s_z} = [0 \quad 0 \quad m_z(n)]^T, \tag{b14}$$

$$\frac{\partial \boldsymbol{\mu}(n)}{\partial \alpha_{xy}} = [m_y(n) \quad m_x(n) \quad 0]^T, \tag{b15}$$

$$\frac{\partial \boldsymbol{\mu}(n)}{\partial \alpha_{xz}} = [m_z(n) \quad 0 \quad m_x(n)]^T, \tag{b16}$$

$$\frac{\partial \boldsymbol{\mu}(n)}{\partial \alpha_{yz}} = [0 \quad m_z(n) \quad m_y(n)]^T. \tag{b17}$$

Define

$$\mathbf{F}(n) \triangleq \left[\frac{\partial \boldsymbol{\mu}(n)}{\partial b_x} \quad \frac{\partial \boldsymbol{\mu}(n)}{\partial b_y} \quad \frac{\partial \boldsymbol{\mu}(n)}{\partial b_z} \quad \frac{\partial \boldsymbol{\mu}(n)}{\partial s_x} \quad \frac{\partial \boldsymbol{\mu}(n)}{\partial s_y} \quad \frac{\partial \boldsymbol{\mu}(n)}{\partial s_z} \quad \frac{\partial \boldsymbol{\mu}(n)}{\partial \alpha_{xy}} \quad \frac{\partial \boldsymbol{\mu}(n)}{\partial \alpha_{xz}} \quad \frac{\partial \boldsymbol{\mu}(n)}{\partial \alpha_{yz}}\right], \tag{b18}$$

which can be written as

$$\mathbf{F}(n) = \begin{bmatrix} 1 & 0 & 0 & m_x(n) & 0 & 0 & m_y(n) & m_z(n) & 0 \\ 0 & 1 & 0 & 0 & m_y(n) & 0 & m_x(n) & 0 & m_z(n) \\ 0 & 0 & 1 & 0 & 0 & m_z(n) & 0 & m_x(n) & m_y(n) \end{bmatrix}. \tag{b19}$$

The CRBs are a set of inequalities stating that, provided the estimates are unbiased, the covariance matrix of the estimated parameter vector is lower bounded by the inversed Fisher information matrix, as shown in reference (17)

$$[FIM]_{ij} = \frac{1}{2} N \cdot \mathrm{tr}[\mathbf{Q}^{-1}\mathbf{Q}_i'\mathbf{Q}^{-1}\mathbf{Q}_i'] + \sum_{n=1}^{N}\left[\boldsymbol{\mu}(n)_i'^T \mathbf{Q}^{-1}\boldsymbol{\mu}(n)_j'\right], \tag{b20}$$

where $\mathbf{X}_i'$ denotes the derivative of $\mathbf{X}$ with respect to the *i*th unknown parameter and $\mathbf{Q}$ denotes the noise covariance matrix. Since $\mathbf{Q}$ does not depend on any parameter in $\boldsymbol{\theta}$, the CRB can be derived based on the second term of the right side of equation (b20) as

$$\mathrm{CRB}(\boldsymbol{\theta}) = [\textstyle\sum_{n=1}^{N}(\mathbf{F}(n)^T\, \mathbf{Q}^{-1}\mathbf{F}(n))]^{-1}. \tag{b21}$$

Assuming $\mathbf{Q} = \sigma^2\mathbf{I}$ with $\mathbf{I}$ being 3x3 identity matrix, the CRBs can be simplified as

$$\mathrm{CRB}(\boldsymbol{\theta}) = \sigma^2[\textstyle\sum_{n=1}^{N}(\mathbf{F}(n)^T\, \mathbf{F}(n))]^{-1}, \tag{b22}$$

which can easily be numerically evaluated.

### C. Estimation Method for Pitch and Roll Misalignment Angles

Assume the top surface of the turntable aligns accurately with the x-y plane of the local level frame. However, mounting the smartphone on the table can introduce a misalignment between the magnetometer body frame and the local level frame, characterized by small values of pitch

($\theta$) and roll ($\varphi$) angles. Then, the transformation of the measured magnetic field from the body frame to the local level frame at each station can be expressed below, according to reference (18)

$$\begin{bmatrix} m_x^l(k) \\ m_y^l(k) \\ m_z^l(k) \end{bmatrix} = \begin{bmatrix} \mathrm{c}(\theta) & 0 & \mathrm{s}(\theta) \\ 0 & 1 & 0 \\ -\mathrm{s}(\theta) & 0 & \mathrm{c}(\theta) \end{bmatrix} \begin{bmatrix} 1 & 0 & 0 \\ 0 & \mathrm{c}(\varphi) & -\mathrm{s}(\varphi) \\ 0 & \mathrm{s}(\varphi) & \mathrm{c}(\varphi) \end{bmatrix} \cdot \begin{bmatrix} m_x(k) \\ m_y(k) \\ m_z(k) \end{bmatrix}, \quad k = 1,2,\dots,K \tag{c1}$$

where $\mathrm{c}(\cdot) = \cos(\cdot)$ and $\mathrm{s}(\cdot) = \sin(\cdot)$; $m_x^l(k), m_y^l(k)$, and $m_z^l(k)$ denote magnetometer measurements in the local level frame; $K$ is the total number of heading stations. Define the horizontal component of the estimated magnetic measurements in the local level frame as

$$H(k) = \mathrm{sqrt}\left(\left(\hat{m}_x^l(k)\right)^2 + \left(\hat{m}_y^l(k)\right)^2\right), \quad k = 1,2,\dots,K. \tag{c2}$$

With a valid misalignment compensation, the horizontal component $H(k)$ of the magnetometer measurements should be a constant value that is independent of heading stations. Therefore, the estimates of $\theta$ and $\varphi$ can be obtained by minimizing the following cost function.

$$f(\theta,\varphi) \triangleq \max_{1\le k\le K}\left(H(k)\right) - \min_{1\le k\le K}\left(H(k)\right). \tag{c3}$$

In this work, instead of estimating pitch and roll misalignment parameters simultaneously, we used the 1D golden-section search method to optimize $\theta$ and $\varphi$ separately (14). We repeated this process iteratively until results converged.